



# Amino-rich Ag-NWs/NH<sub>2</sub>-MIL-125(Ti) hybrid heterostructure via LSPR effect for photo-assist uranium extraction from fluorine-containing uranium wastewater without sacrificial agents

Boyuan Tu<sup>a,1</sup>, Kaifu Yu<sup>a,b,1</sup>, Dengjiang Fu<sup>a</sup>, Li Zhou<sup>a</sup>, Ruixiang Wang<sup>a</sup>, Xinying Jiang<sup>a</sup>, Huanhuan Liu<sup>a</sup>, Xin Cao<sup>a</sup>, Xiang Gong<sup>a</sup>, Rong He<sup>a</sup>, Yongjian Tang<sup>a</sup>, Tao Chen<sup>a,\*</sup>, Wenkun Zhu<sup>a,\*</sup>

<sup>a</sup> State Key Laboratory of Environment-friendly Energy Materials, National Co-innovation Center for Nuclear Waste Disposal and Environmental Safety, Sichuan Civil-military Integration Institute, School of National Defense & Nuclear Science and Technology, School of Mathematics and Physics, Southwest University of Science and Technology, Mianyang, Sichuan 621010, PR China

<sup>b</sup> College of Chemistry, Sichuan University, Chengdu, Sichuan 610064, PR China

## ARTICLE INFO

### Keywords:

Ag nanowires  
NH<sub>2</sub>-MIL-125(Ti)  
U(VI)

Photo-assist uranium extraction

## ABSTRACT

Photo-assist uranium extraction from fluorine-containing uranium wastewater by building semiconductor-plasma material heterostructure is a forward-looking strategy, which not only effectively accelerates F-U separation via the LSPR effect but also impacts the intensity of binding between U(VI) and site. Here, we developed an amino-rich Ag-NWs/NH<sub>2</sub>-MIL-125(Ti) (AgNW/N-M(Ti)) hybrid nanowires with LSPR effect for photo-assist uranium extraction. Accordingly, the AgNW/N-M(Ti) hybrid nanowires presented 90.4% removal efficiency for U(VI) without a sacrificial agent at the U: F molar ratio of 1:20. By virtue of In-situ KPFM, we identify hot electrons generated over AgNW were transferred to amino-rich N-M(Ti) to efficiently reduce the U(VI) adsorbed on the N-M(Ti), which effectively enhances the excellent uranium removal performance of AgNW/N-M(Ti) hybrid nanowires. This strategy may open a paradigm for the development of advanced heterojunctions with the LSPR effect as catalysts for photo-assisted uranium extraction from fluorine-containing uranium wastewater.

## 1. Introduction

As the industry of nuclear energy rapidly develops, uranium-contained effluent is ineluctably generated [1,2]. Enriching and recovering uranium in radioactive effluent is particularly important for environmental protection and the sustainable development of nuclear energy [3–7]. In particular, nuclear industrial production processes, such as uranium enrichment, uranium conversion, and fuel element manufacturing, will produce much high-fluorine uranium-containing wastewater. The uranium extraction from high-fluorine uranium-containing wastewater becomes more difficult because fluoride and uranyl ions are easy to form complexes, such as UO<sub>2</sub>F<sup>+</sup>, UO<sub>2</sub>F<sub>2</sub>(aq), and UO<sub>2</sub>F<sub>3</sub> [8–15]. As a consequence, the development of a method for efficient uranium enrichment in high-fluorine environment is an imminent issue to properly solve the problem of uranium wastewater produced by the nuclear industry.

Photo-assisted uranium extraction, as a simple and environmentally friendly new technology, is widely employed in wastewater. Notably, the photo-assisted uranium extraction technology can convert soluble U(VI) into more stable U(IV) [16], which is expected to solve the problem of F-U separation in fluorine-containing uranium wastewater. MIL-125(Ti), as a new metal-organic framework (MOF) material, has attracted much attention due to excellent stability, adjustable pore structure, high specific surface area, and excelled photocatalytic reduction activity that MIL-125(Ti) possessed [17]. For example, the Nb<sub>2</sub>O<sub>5</sub>@MIL-125 hybrid materials have been reported to be utilized for photo-assisted extraction of hexavalent chromium from industrial wastewater [18]. However, the light absorption and reaction kinetics of MIL-125(Ti) are not satisfactory in the actual wastewater treatment process. The local surface plasmon resonance (LSPR) effect in multiphase photocatalysis is a proactive branch that effectively decreases the compounding efficiency of high-energy hot electrons with holes and thus promotes the smooth

\* Corresponding authors.

E-mail addresses: [chent@swust.edu.cn](mailto:chent@swust.edu.cn) (T. Chen), [zhuwenkun@swust.edu.cn](mailto:zhuwenkun@swust.edu.cn) (W. Zhu).

<sup>1</sup> These authors contributed equally to this work.

progress of redox reactions [16,19]. Considering that hot electron injection arising from the plasma effect not only impact the intensity of binding between U (VI) and site but also accelerate the F-U complex to pass through the Coulomb effect [20]. Therefore, the hybrid of MIL-125 (Ti) and plasma material was potential for selective and high-efficiently extracting uranium from fluorine-containing uranium wastewater.

Herein, amino-rich  $\text{NH}_2\text{-MIL-125(Ti)}$  hybrid Ag nanowires (AgNW/N-M(Ti)) heterostructure was developed via a convenient and environmentally friendly hydrothermal synthesis. N-M(Ti) of Surface-grown amino groups was hydrothermally driven to bind in situ to Ag nanowires filled with hot electrons charged at the interface. The interfacial transported hot electrons not only enhanced the charge carrier separation efficiency at the binding sites of N-M(Ti) and U(VI) represented by amino groups but also the efficient utilization of light energy due to the photothermal synergistic effect of the high-energy excited hot electrons together with the excited photoelectrons. By In-situ KPFM assessment of the change in potential on the surface of the composite, combined with other spectroscopic analyses, we found this hybrid nanowire effectively enhanced the separation of hole electron pairs indeed, while the amino groups provide active sites for the capture of uranyl ions. This semiconductor-plasma material heterostructure possessed excellent U (VI) removal efficiency over a wide range of U(VI) concentrations. Noteworthily, fluoride ions, as a detrimental factor for U(VI) removal in conventional radioactive effluent, to some extent, barely impacted uranium extraction via AgNW/N-M. This work presented a novel draft for the design of advanced heterojunctions with the LSPR effect as catalysts for photo-assisted uranium extraction from fluorine-containing uranium wastewater.

## 2. Materials and methods

### 2.1. Chemicals

Acetone ( $\text{C}_3\text{H}_8\text{O}$ , 99.8%, AR), Tetrabutyl titanate [ $\text{Ti}(\text{OC}_4\text{H}_9)_4$ , 99.0%, AR], silver nitrate ( $\text{AgNO}_3$ , 99.0%, ACS), 2-aminoterephthalic acid ( $\text{C}_8\text{H}_7\text{NO}_4$ , 98.0%, HPLC), N,N-Dimethylformamide ( $\text{C}_3\text{H}_7\text{NO}$ , 99.8%, ACS), and methanol ( $\text{CH}_3\text{OH}$ , 99.5%, AR), were purchased from Aladdin. Polyvinylpyrrolidone [ $[(\text{C}_6\text{H}_9\text{NO})_n]$ , M.W.  $\sim 40\ 000$ ], Sodium chloride ( $\text{NaCl}$ , 99.5%, AR), Glycerol ( $\text{C}_3\text{H}_8\text{O}_3$ , 99%, AR), Hydrochloric acid ( $\text{HCl}$ , 36–38%, AR) and Sodium hydroxide ( $\text{NaOH}$ , 98%, AR) were obtained from Shanghai Macklin Biochemical Technology Co., Ltd. All chemicals were used directly without purification.

### 2.2. Synthesis of silver nanowires by polyol method

In a typical experiment, 4 mL glycerol solution, 5 mL PVP solution (M.W.  $\sim 40\ 000$ , 60 mg/mL), and 0.5 mL of 0.1 M  $\text{NaCl}$  (99.5%) were prepared in advance, then the three kinds of solutions were added in order into the beaker. 0.465 mL of 1 M  $\text{AgNO}_3$  was freshly prepared just before use. The  $\text{AgNO}_3$  solution was dropped into the beaker and stirred at a rate of 1000 rpm. Temperature setting from 60 °C to 210 °C within 15 min in the oil bath to obtain the nanowires. The obtained silver nanowires after the reaction were condensed in deionized water and finally separated by centrifugation with acetone and ethanol, respectively.

### 2.3. Synthesis of $\text{NH}_2\text{-MIL-125(Ti)}$ and Ag-NWs/ $\text{NH}_2\text{-MIL-125(Ti)}$

$\text{Ti}(\text{OC}_4\text{H}_9)_4$  (2.4 mL), 2-aminoterephthalic acid (2.2 g), N,N-Dimethylformamide (36.0 mL), and  $\text{CH}_3\text{OH}$  (4.0 mL) were added respectively in a Teflon reactor and heated to 150 °C for 48 h. The precipitate was measured with centrifugal separation and rinsed several times with methanol to remove the residuary N,N-Dimethylformamide. Then, the obtained samples were dried under a vacuum situation at 60 °C for 2 h to get the powder and heated to 180 °C in the same situation to remove the residuary 2-aminoterephthalic acid. Furthermore,

incorporated the as-prepared Ag-NWs (10 mg) into 4.0 mL methanol solution to replace the methanol mentioned previously and synthesized the AgNW/N-M(Ti) under the same conditions as the N-M(Ti).

### 2.4. Photocatalysis experiments

AgNW/N-M(Ti) and N-M(Ti) were prepared in advance and used as catalysts for the photo-assisted reduction of hexavalent uranium. With no specification, all the reactions occurred in the air atmosphere with 20 mL solutions, 5 mg catalysts, and no sacrificial agents. And prepared the solutions of hexavalent uranium ( $C_{\text{UO}_2^{2+}} = 1\ \text{ppm}$ , 8 ppm, 20 ppm, 50 ppm, 100 ppm, 200 ppm). Photocatalytic experiments were measured with a simulated light source (xenon lamp). To maintain the adsorption-desorption balance, the mixed solution was agitated and retained in the dark condition for about 30 min ahead of the photocatalysis process. Besides, the effects of anti-ion interference were evaluated ( $C_{\text{U(VI)}}: C_{\text{Interfering}} = 1: 1$ , interfering ions as  $\text{Na}^+$ ,  $\text{K}^+$ ,  $\text{Ca}^{2+}$ ,  $\text{Mg}^{2+}$ ,  $\text{Sr}^{2+}$ ,  $\text{Zn}^{2+}$ ).

After the photocatalysis, the quantities of  $\text{UO}_2^{2+}$  were measured by UV-Vis (wavelength of 651.8 nm).

A formula following as the determining of the ratio of U(VI) removal during photocatalysis:

$$\text{removal ratio} = \frac{C_0 - C_t}{C_0} \times 100\%$$

In this formula,  $C_0$  takes for the initial  $C_{\text{U(VI)}}$ , and  $C_t$  takes for the  $C_{\text{U(VI)}}$  while photocatalysis processing.

## 3. Results and discussion

The process of synthesizing AgNW/N-M(Ti) hybrid nanowire is schematically illustrated in Fig. 1a. To begin with, the pristine Ag nanowires (Ag-NWs) were obtained by a simple polyol method referring to the previous reports [21,22]. Afterward, the Ag-NWs were uniformly dispersed in the solution containing  $\text{NH}_2\text{-BDC}$ ,  $\text{Ti}(\text{OC}_4\text{H}_9)_4$ , DMF, and MeOH with the assistance of ultrasound. And the above miscible liquids were delivered to a Teflon lining container and maintained at 150 °C for 24 h. Finally, AgNW/N-M(Ti) hybrid nanowires were successfully prepared with N-M(Ti) nanosheets supported on the Ag-NWs. The morphology of the AgNW/N-M(Ti) hybrid nanowire and Ag-NWs were identified by SEM and TEM (Fig. S1&S2). The TEM image of AgNW/N-M(Ti) exhibited  $^1\text{D}-2^{\text{D}}$  hybrid structure (Fig. 1b). Fig. 1c shows the HRTEM image of AgNW/N-M(Ti) hybrid nanowires over the nanowire region. The 2.056 Å interplanar spacing of characteristic lattice fringe was attributed to the (200) facet of Ag-NWs. Fig. 1d show the morphology image and corresponding energy dispersive X-ray elemental mapping images (TEM-EDX) of AgNW/N-M(Ti). The signal of the N element and Ti element overlaid at the entire region of the nanoflakes region, and the signal of Ag integrally existed in the nanowire region yet. The above results further confirmed that N-M(Ti) nanoflakes were successfully coated on the surface of Ag-NW.

In order to investigate the crystal structure and electronic structure of the AgNW/N-M(Ti) hybrid nanowire, we further performed XRD, XPS, and FT-IR spectrum measurements. As displayed in the XRD patterns (Fig. 1e), the AgNW/N-M(Ti) hybrid nanowire exhibited the featured peaks of N-M(Ti) and metallic Ag (PDF#04-0783) [23–25], further verifying the successful fabrication of AgNW/N-M(Ti) hybrid nanowires. The Ag 3d XPS spectra of Ag-NW exhibited two characteristic peaks located at 367.62 and 373.62 eV, which were attributed to Ag  $3d_{5/2}$  and Ag  $3d_{3/2}$  [26]. Compared with pure Ag-NW, the Ag 3d XPS spectra of the AgNW/N-M(Ti) hybrid nanowire shifted slightly to the high-E region due to electron transfer after hybridization (Fig. 1f). As Fig. 1g displayed, Ti 2p was deconvoluted into two components, conformed to Ti  $2p_{1/2}$  and Ti  $2p_{3/2}$ , respectively [24,25,27]. Notably, the Ti 2p XPS spectra of AgNW/N-M(Ti) hybrid nanowire shifted slightly to the

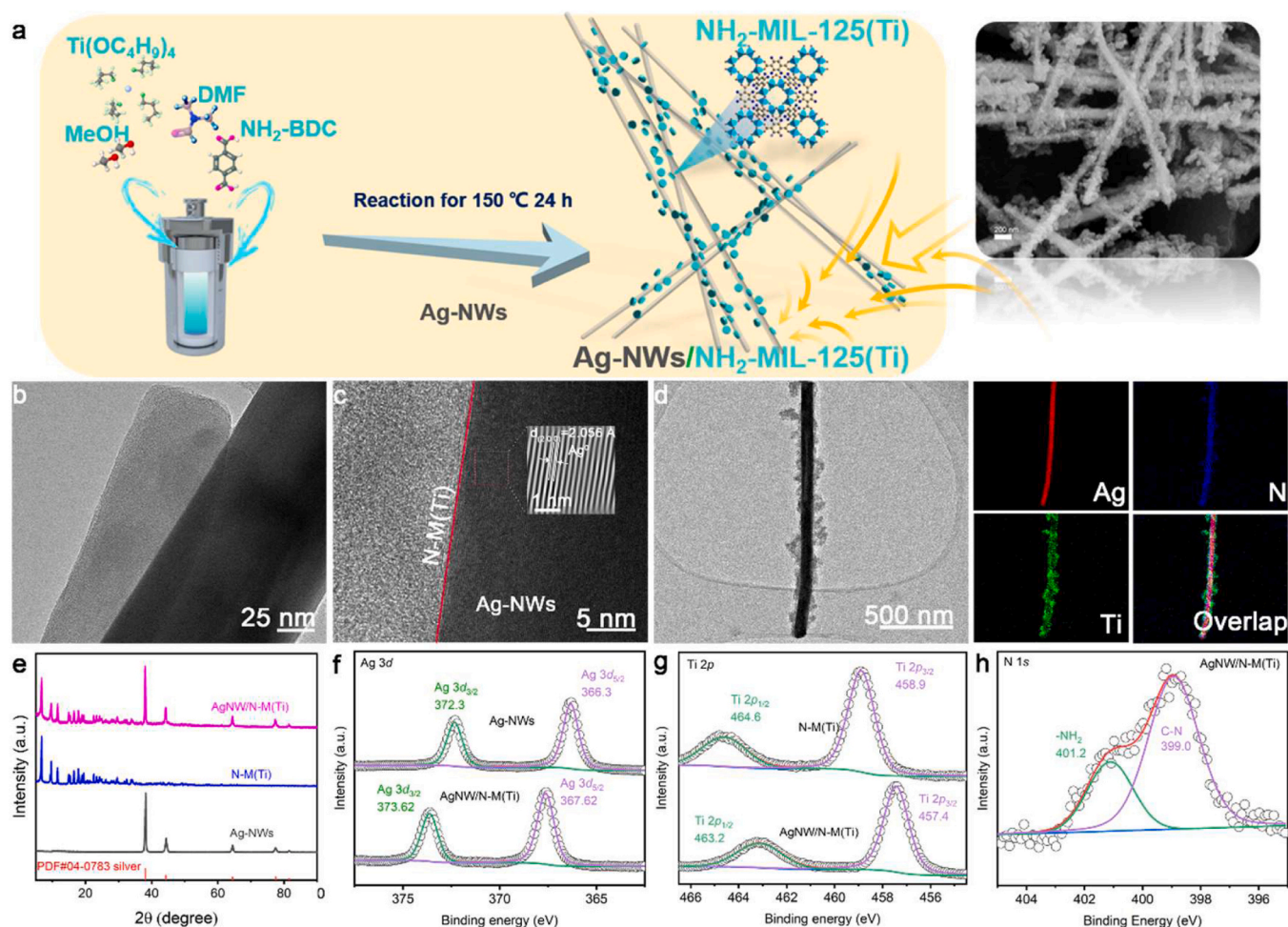


**Fig. 1.** (a) Fabrication process of the AgNW/N-M(Ti). (b) TEM image of AgNW/N-M(Ti). (c) HRTEM image of AgNW/N-M(Ti). (d) The image of TEM and corresponding TEM-EDX elemental mapping images of AgNW/N-M(Ti). (e) XRD patterns of Ag-NWs, N-M(Ti) and AgNW/N-M(Ti). The XPS spectra of (f) Ag 3d, (g) Ti 2p, and (h) N 1s.

low- $E$  region with regard to pristine N-M(Ti), further confirming the result of hot electron transfer from Ag-NW to N-M(Ti) after hybridization. As shown in Fig. 1h, the N 1s XPS spectra of AgNW/N-M(Ti) hybrid nanowire displayed the two peaks located at 401.2 and 399.0 eV, which were ascribed to the  $-NH_2$  and C-N bonds, respectively [27], identifying the retention of nitrogen-containing functional groups in N-M(Ti) after hybridization. As Fig. S3 showed, the FT-IR spectra of N-M(Ti) and AgNW/N-M(Ti) hybrid nanowires [25]. The AgNW/N-M(Ti) hybrid nanowires still retained abundant nitrogen-containing functional groups (e.g.,  $-NH_2$ ) after hybridization, which furnished a huge number of active sites to the selective capture of U(VI).

### 3.1. Optical and electronic properties

To further demonstrate the excellent capacity of AgNW/N-M(Ti) with regard to U(VI) photoreduction, testing the optical and electronic properties with measures to be evaluated. With regard to Fig. 2a, the UV-vis spectra showed the specific tendency of peaks to the as-prepared samples. Due to the localized surface plasmon resonance effect of Ag-NWs, the absorption curve of AgNW/N-M(Ti) is almost higher than that of N-M(Ti) with a wavelength coverage of 200–800 nm. On referring to the Tauc/Davis–Mott model, the  $E_g$  (band gap width) of the original N-M(Ti) was 2.65 eV where  $E_{VB}$  and  $E_{CB}$  were 2.13 eV and  $-0.52$  eV inferring from the valence spectrum, respectively. And the Schottky barrier was generated at the boundary due to the contacting between N-M(Ti) and Ag-NWs (Fig. 2b). The hot electrons produced due

to the LSPR effect were transferred from Ag-NWs through the Schottky barrier up to the conduction band of N-M(Ti) for further reduction of trapped  $UO_2^{2+}$  [28]. According to the reports, the separation of hot electron-hole pairs were boosted efficiently due to the hybrid structure of AgNW/N-M(Ti) [29,30]. This demonstration was confirmed by steady-state photoluminescence spectroscopy (PL) with an excitation wavelength of 325 nm (Fig. 2c). The lower PL intensity of AgNW/N-M(Ti) indicated the higher efficiency of carrier separation led to an enhancement of photocatalytic activity. In addition, N-M(Ti) has a significant PL peak near 470 nm, which is attributed to the contribution of Eg ( $\sim 2.65$  eV). Furthermore, the lightly blue shift of AgNW/N-M(Ti) in the PL spectra was contributed to the pyrrolic-like nitrogen atoms introduced from the synthesis of Ag-NWs with polyvinylpyrrolidone [31,32]. In order to assess the photon-to-electron transition, transient photocurrent responses via AgNW/N-M(Ti) and N-M(Ti) were evaluated via the photoelectrochemical technique. As displayed in Fig. 2d, the signals of N-M(Ti) to photocurrent were nearly negligible, while AgNW/N-M(Ti) exhibited obvious photocurrent signals. The above analysis further demonstrated that the LSPR effect enhanced the light response efficiency of N-M(Ti). To further verify the transfer of the photogenerated electrons transfer, In-situ Kelvin probe force microscopy (In-situ KPFM) was applied to assess the spatial distribution of electric charge [32–37]. A comparison of the surface photovoltage spectra of the material under dark and light-introducing conditions was performed through atomic force microscope image (AFM) (Fig. S6). For details in the 3D AFM images (Fig. 3a1, a2; b1, b2; c1, c2), the surface potential of



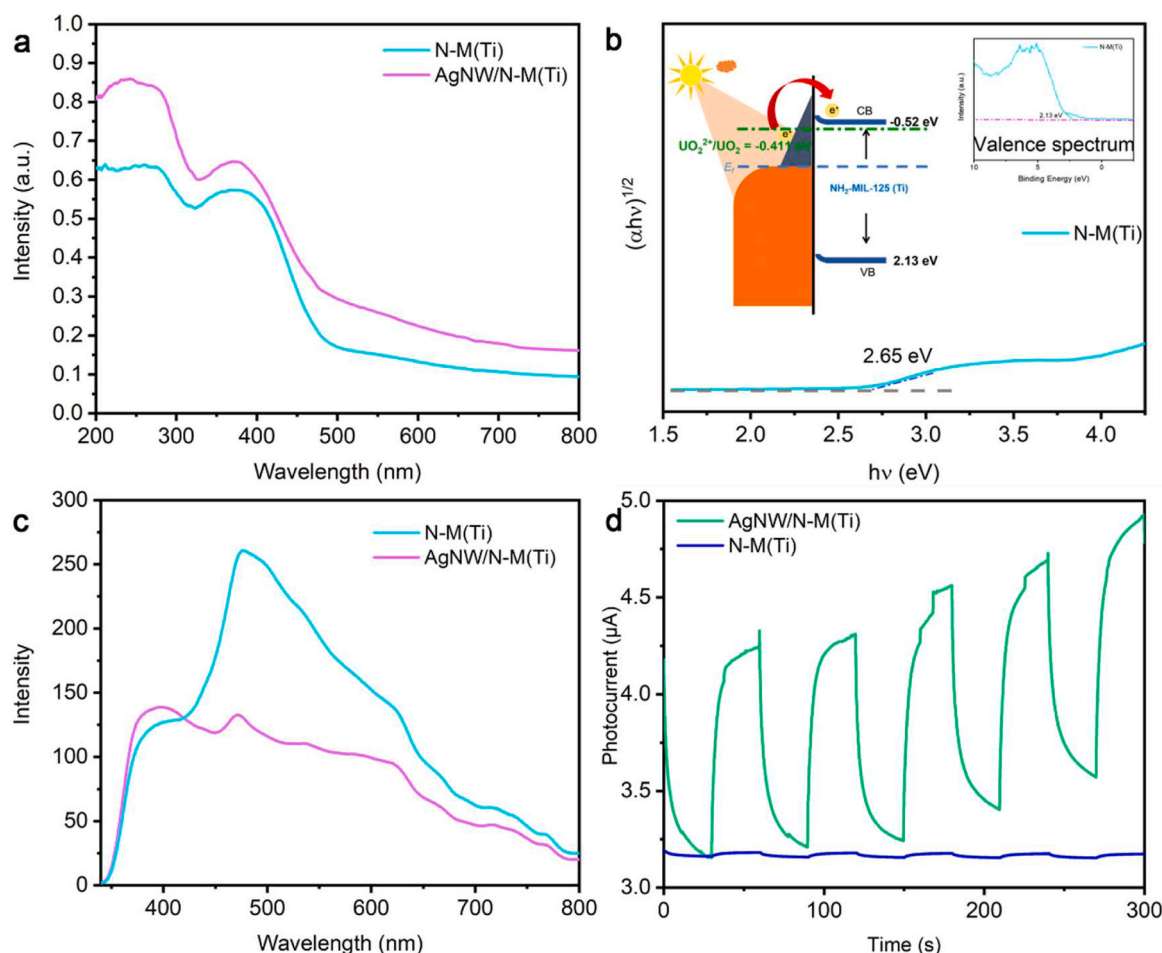


**Fig. 2.** (a) Diffuse reflectance UV-vis spectra of N-M(Ti) and AgNW/N-M(Ti). (b) Schematic diagram, valence spectrum, and  $(\alpha h\nu)^{1/2}$  vs  $h\nu$  curves of the band structures of N-M(Ti). (c) PL spectroscopy in steady-state of N-M(Ti) and AgNW/N-M(Ti). (d) Transient photocurrent responses of N-M(Ti) and AgNW/N-M(Ti).

AgNW/N-M(Ti) at site A increased by  $\sim 11.29$  mV while site B decreased by  $\sim 1.9$  mV from dark to light comparing in the surface photovoltage spectra (SPV), indicating that the process of electron transferred from site A to site B was generated with the introducing of light [38,39]. However, monomeric N-M(Ti) and Ag-NWs exhibited a decrease in the overall electric potential without the same electron transferring as AgNW/N-M(Ti). In addition, N-M(Ti) (the surface potential shift  $\sim -73.55$  mV in dark and  $-72.03$  mV in light) and Ag-NWs (the surface potential shift  $\sim -35.09$  mV in dark and  $-34.18$  mV in light) possessed lower shift than that of AgNW/N-M(Ti) (the surface potential shift  $\sim -117.93$  mV in dark and  $-131.12$  mV in light), further confirming the transfer of hot electrons on Ag-NWs to N-M(Ti).

In addition, we further investigated the light absorption capacity of AgNW/N-M(Ti) by the detection of infrared thermal imager with the irradiation using a xenon lamp (Fig. 3(a3-a6)) and using ethanol as a dispersant to disperse AgNW/N-M(Ti) uniformly on the conductive glass and detecting the temperature change of the conductive glass over time (18 s, 45 s, 120 s, and 206 s). As shown in the infrared thermal images, AgNW/N-M(Ti) has the fastest temperature increase compared to Ag-NWs and N-M(Ti) at the same time, indicating that AgNW/N-M(Ti) has better photothermal ability (Fig. 3(b3-b6; c3-c6)).

### 3.2. Photocatalytic performance

The AgNW/N-M(Ti) hybrid nanowires with hot electron injection provided an ideal platform for revealing the effect of the plasma effect on enhancing uranium extraction [16]. Fig. 4a indicates the reaction time profile of Ag-NWs, N-M(Ti), and AgNW/N-M(Ti) with/without

simulated sunlight assistance [40]. In the condition of no light, the Ag-NWs showed barely catalytic activity toward U(VI) photoreduction. After the hybrid N-M(Ti), the AgNW/N-M(Ti) showed significant uranium extraction performance, and the removal rate reached 67.6%. When the system was exposed to light, the photocatalytic performance of AgNW/N-M(Ti) for U(VI) was 90.4%, much higher pristine N-M(Ti) (68.3%) and Ag-NWs after irradiation for 60 min, indicating that hot electrons generated by the localized surface plasmon resonance can effectively enhance the extraction of U(VI). In order to further understand the mechanism of the enhancement of uranium extraction efficiency by the plasma effect, the reaction kinetic constant ( $k$ ) is further calculated based on the pseudo-first-order kinetic equation ( $-\ln(C/C_0) = kt$ , where  $C_0$  and  $C_t$  respectively represent the U(VI) concentration at different reaction times respectively) [41]. As shown in Fig. 4b, the  $k$  values for Ag-NWs, N-M(Ti), and AgNW/N-M(Ti) were AgNW/N-M(Ti) ( $0.0372 \text{ min}^{-1}$ ) > N-M(Ti) ( $0.0184 \text{ min}^{-1}$ ) > Ag-NWs ( $0.0004 \text{ min}^{-1}$ ), respectively. The aforementioned findings demonstrate that the critical aspect of the photo-assisted uranium extraction process is the localized surface plasmon resonance.

AgNW/N-M(Ti) also performed equally well in terms of catalytic activity compared to previously reported catalysts for the photoreduction of U(VI) (Fig. S15, Table S1). AgNW/N-M(Ti) was used as a photocatalyst for U(VI) concentration, and the effect of initial U(VI) concentration, pH value, U : F ratio and competitive cation on the uranium extraction was further carried out. As shown in Fig. 4c, the AgNW/N-M(Ti) maintained ideal uranium extraction capacity in the range of uranium concentration of 1–200 mg/L. Despite the fact that the initial uranium concentration reached 200 mg/L, the AgNW/N-M(Ti)



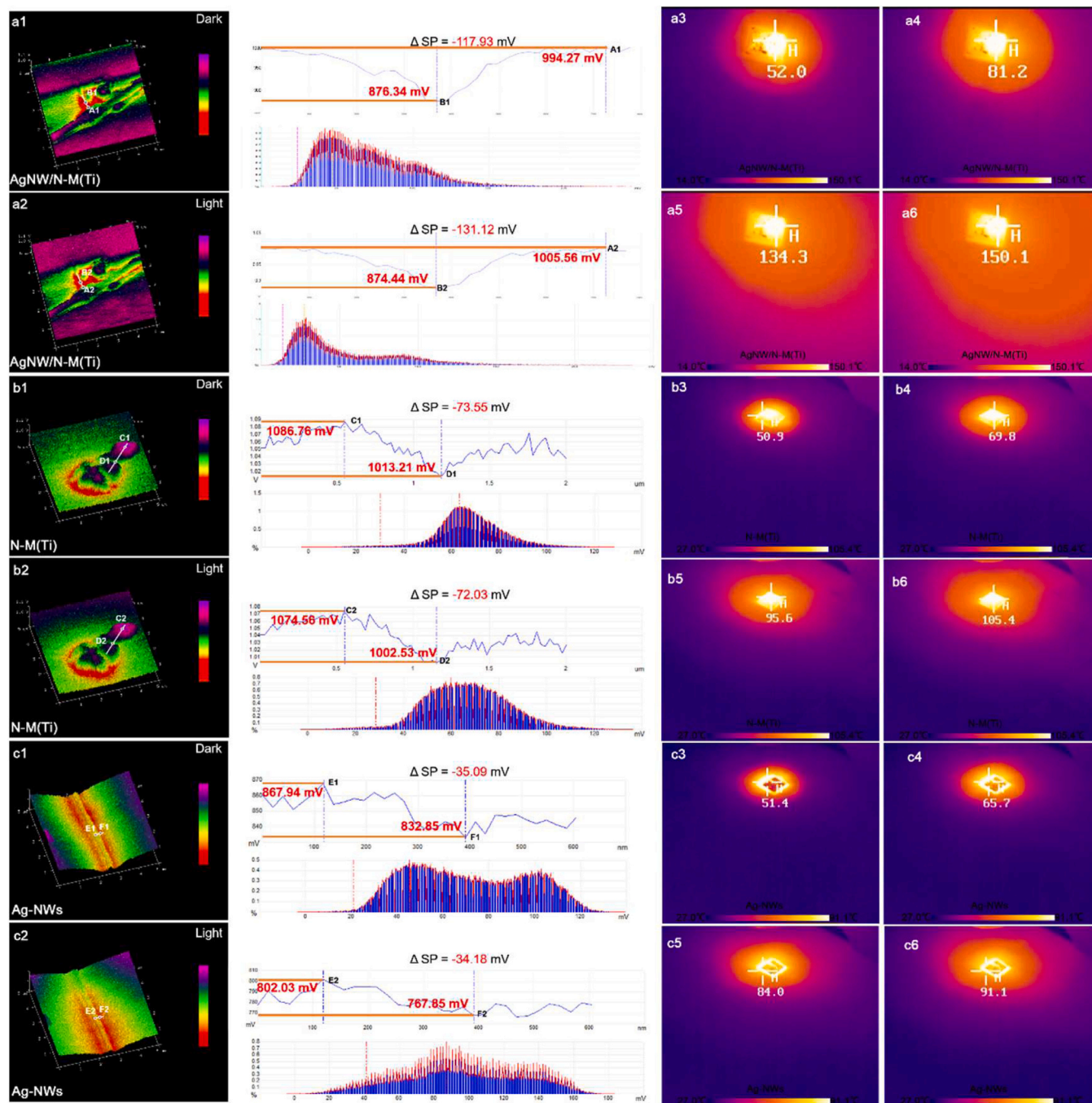


**Fig. 3.** (a1, a2; b1, b2; c1, c2) 3D surface potential maps and the corresponding surface photovoltage spectra in the light-dark contrast cases of AgNW/N-M(Ti), N-M(Ti) and Ag-NWs. (a3, a4, a5, a6; b3, b4, b5, b6; c3, c4, c5, c6) The infrared thermal images of AgNW/N-M(Ti), N-M(Ti) and Ag-NWs under irradiation using a xenon lamp.

nevertheless demonstrated a comparatively high removal rate of 79.8% for U(VI) with the uranium extraction capacity reaching 638.4 mg/g. Moreover, AgNW/N-M(Ti) possessed outstanding performance in U(VI) removal ratios at pH from 3 to 10 (Fig. 4d), showing satisfactory environmental applicability [42]. As for the influence of F<sup>-</sup> in U(VI) photoreduction via AgNW/N-M(Ti) (Fig. 4e), a series of experiments designed by the mole ratio of U: F on the U(VI) removal ratio was taken. And the removal ratio of uranium by AgNW/N-M(Ti) remained at a high level during the period when the molar concentration of F<sup>-</sup> was 20 times that of UO<sub>2</sub><sup>2+</sup>. To measure the selectivity of AgNW/N-M(Ti) in the system of U(VI) reduction, a series of cations (including Na<sup>+</sup>, K<sup>+</sup>, Ca<sup>2+</sup>, Mg<sup>2+</sup>, Sr<sup>2+</sup>, Zn<sup>2+</sup>) were introducing into photocatalytic reduction (Fig. 4f) [43]. In

the presence of interfering metal ions, the removal rate of uranium by AgNW/N-M(Ti) exceeded 90%, which is due to the enhanced capture and reduction of UO<sub>2</sub><sup>2+</sup> by hot electron injection [16]. Accordingly, we further characterized the crystal structure of the AgNW/N-M(Ti) after U(VI) photoreduction. The structural integrity of AgNW/N-M(Ti) were well maintained after the reaction, further confirming the excellent stability of the AgNW/N-M(Ti). Notably, the peak of UO<sub>4</sub>·4 H<sub>2</sub>O (JCPDS: 00-016-0206) were clearly displayed in the XRD spectrum of AgNW/N-M(Ti) after U(VI) photoreduction (Fig. S7). In addition, the AgNW/N-M(Ti) still possessed a considerable removal ratio of 80.76% after five cycles (Fig. S8) [44]. Based on the above analysis, we have the cause to conclude that introducing localized surface plasmon resonance

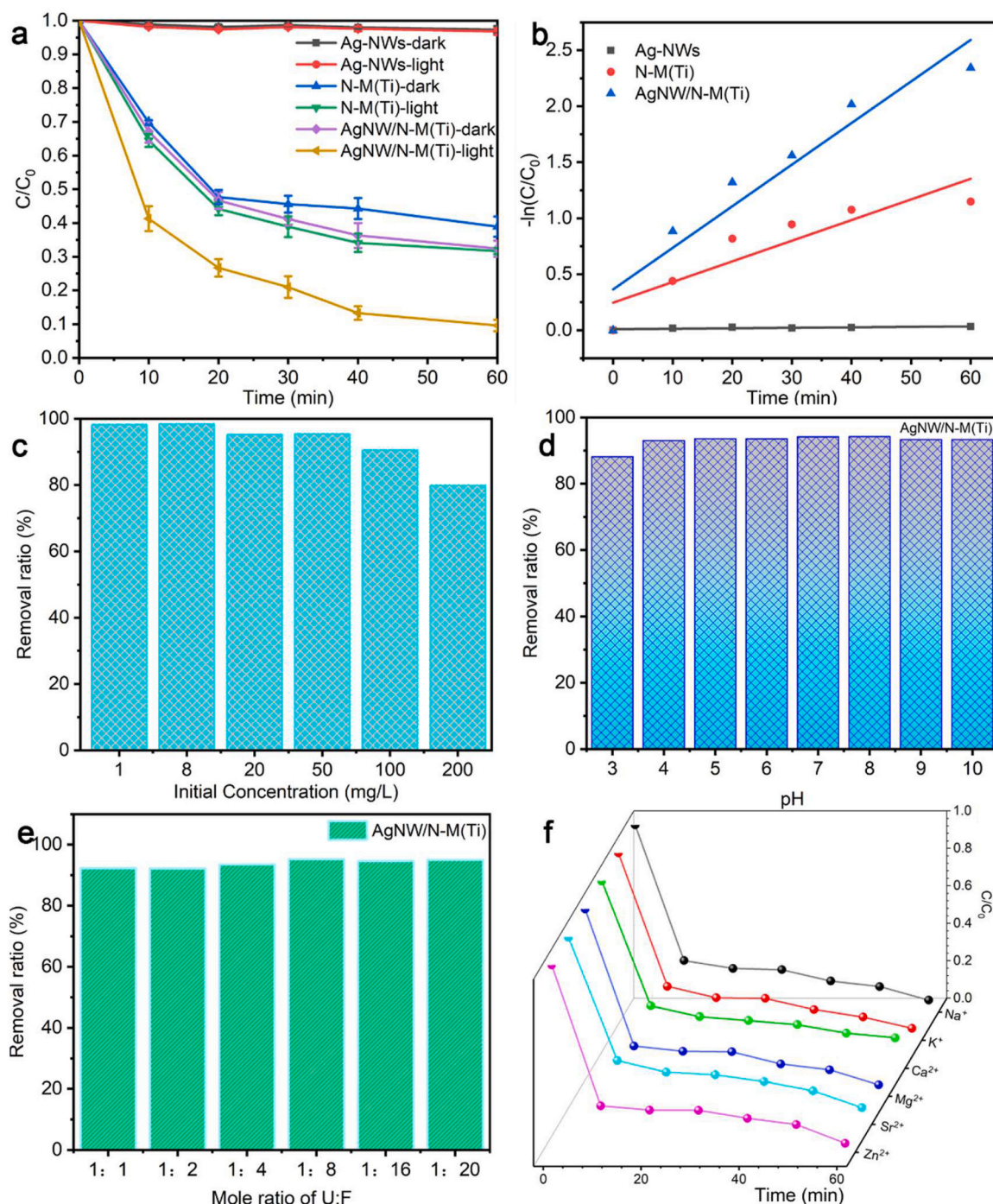


**Fig. 4.** (a) Curves of light-assisted catalytic reduction performance of U(VI) vs time via Ag-NWs, N-M(Ti) and AgNW/N-M(Ti) after 60 min with/without light irradiation ( $C_{U(VI)} = 100$  mg/L,  $T = 293$  K,  $pH = 7$ ). (b) Plots of Pseudo-first-order kinetic with the above samples. (c) Histogram on removal ratio of AgNW/N-M(Ti) with different initial concentrations of U(VI) solutions. (d) Histogram on removal ratio of AgNW/N-M(Ti) in solutions of different pH. (e) Histogram on removal ratio of AgNW/N-M(Ti) in solution with different mole ratios of U: F. (f) The effect of interfering ions on U(VI) concentration at time profile of AgNW/N-M(Ti).

in the process of photo-assisted uranium extraction is a potential approach for efficient uranium extracting [45–48].

### 3.3. Photocatalytic reduction mechanism

To further investigate the photocatalytic mechanism, the enriched products on AgNW/N-M(Ti) were tested by the characterizing method of XPS measurements in dark and light-introducing conditions [49]. The AgNW/N-M(Ti) after uranium extraction under dark and light conditions were called AgNW/N-M(Ti)-U-Dark and AgNW/N-M(Ti)-U-Light,

respectively. As shown in the full XPS spectra of AgNW/N-M(Ti)-U-Dark and AgNW/N-M(Ti)-U-Light (Fig. S9), the U 4f signals were clearly observed. And the four typical characteristic peaks were fitted for the U 4f XPS spectrum (Fig. 5a), corresponding to U(VI) at 391.5 and 380.6 eV together with U(IV) at 389.8 and 379 eV, respectively [49–51]. Notably, the main uranium species in AgNW/N-M(Ti)-U-Dark is U(VI). Mixed species of U(IV) and U(VI) exist on AgNW/N-M(Ti)-U-Light, illustrating that some uranium has been reduced by AgNW/N-M(Ti)-U-Light in the process of photo-assisted extraction. As shown in Fig. 5b, the peaks leading to C-N and  $-NH_2$  of



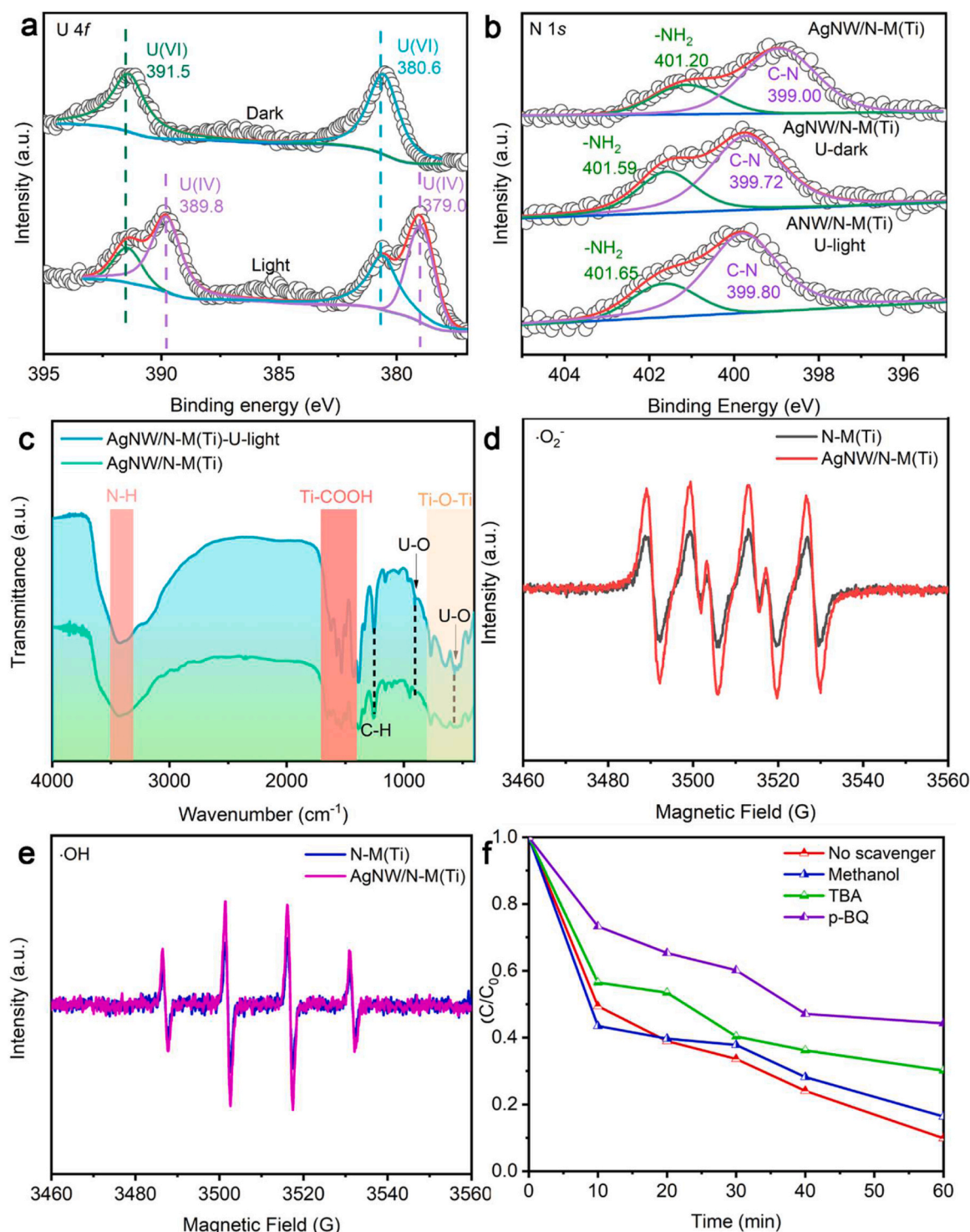


**Fig. 5.** (a) U 4f XPS spectra of AgNW/N-M(Ti)-U-dark and AgNW/N-M(Ti)-U-light. (b) N 1s XPS spectra of AgNW/N-M(Ti), AgNW/N-M(Ti)-U-dark and AgNW/N-M(Ti)-U-light. (c) The FT-IR spectra of N-M(Ti), AgNW/N-M(Ti), AgNW/N-M(Ti)-U-dark and AgNW/N-M(Ti)-U-light. (d) The EPR spectra of  $\cdot\text{O}_2^-$  radicals and (e)  $\cdot\text{OH}$  radicals via N-M(Ti) and AgNW/N-M(Ti) under irradiation using a xenon lamp. (f) The scavengers test towards U(VI) photoreduction of AgNW/N-M(Ti) versus time ( $C_{\text{U(VI)}} = 100 \text{ mg/L}$ ).

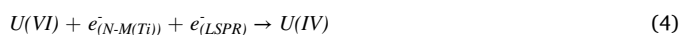
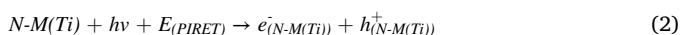
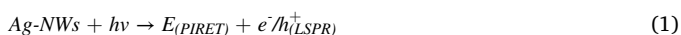
AgNW/N-M(Ti) in the N 1s XPS spectra shifted to higher binding energy with dark and light introducing during the enriching process of uranium, which illustrated that N-M(Ti) as one type of MOFs possess adsorption sites attributing to abundant nitrogenous group [27]. Fig. 5c presented the FTIR of AgNW/N-M(Ti) before and after the reaction. After the reaction, two typical O=U=O antisymmetric vibration peaks at  $908.07 \text{ cm}^{-1}$  and  $567.8 \text{ cm}^{-1}$  appeared in the AgNW/N-M(Ti)-U-Light,

demonstrating the formation of fresh uranium-bearing species which occurred on the surface of AgNW/N-M(Ti) [50]. Meanwhile, the typical absorption bands at  $3389\text{--}3488$ ,  $1400\text{--}1700$ , and  $500\text{--}755 \text{ cm}^{-1}$  corresponded to the -N-H bond and the Ti-carboxyl coordination characteristic vibration and Ti-O-Ti stretching vibration [25,29]. After the adsorption of uranium, the above two absorption bands showed obvious enhancement, which was attributed to the coordination with uranium



[49,50,52].

To investigate the active species for AgNW/N-M(Ti) in the photoreduction, the production of  $\cdot\text{O}_2$  and  $\cdot\text{OH}$  was measured by electron paramagnetic resonance (EPR) with light irradiation. Sequential characteristic peaks of  $\cdot\text{O}_2$  can be observed from the EPR spectra in Fig. 5d. In addition, the intensity of  $\cdot\text{OH}$  signals of AgNW/N-M(Ti) were higher than those of N-M(Ti) (Fig. 5e). And barely EPR signals in the dark condition (Fig. S10). After the hybrid Ag-NWs, stronger  $\cdot\text{O}_2$  signals of AgNW/N-M(Ti) exhibited, compared to those of N-M(Ti), which indicated the photocatalytic of U(VI) was enhanced via AgNW/N-M(Ti) contributed to the production of  $\cdot\text{O}_2$  [53]. In the scavenger tests (Fig. 5f), with visible light irradiating, the photocatalytic reduction capability of U(VI) was assessed. Radicals capture experiments were used to examine the affecting of radicals in the reduction process, in addition, where methanol, tertiary butanol (TBA) (5 mM), and *p*-benzoquinone (*p*-BQ) (5 mM) were introduced into the reaction system as scavengers for holes ( $h^+$ ), hydroxyl radicals ( $\cdot\text{OH}$ ), and superoxide radicals ( $\cdot\text{O}_2$ ), respectively [54–57]. The data of the radicals capture experiments demonstrated that the primary radicals via the AgNW/N-M(Ti) in U(VI) photoreduction led to electrons ( $e^-$ ) and superoxide radicals ( $\cdot\text{O}_2$ ). The early acceleration of the U(VI) photocatalytic kinetics caused by the addition of methanol in the curve, was for the improved efficiency of electron-hole separation due to the valid removal of the hole [55]. Noteworthy, without the adding of a scavenger, AgNW/N-M(Ti) performed well in U(VI) photoreduction. And as the intermediate in water oxidation, hydroxyl radicals scavenged by Tertiary butanol played a role in improving the photocatalytic process. Based on this, we further tested the water oxidation ability of N-M(Ti) and AgNW/N-M(Ti), as shown in Fig. S11. In the LSV curves, AgNW/N-M(Ti) possessed lower potential ( $\sim 1.74$  V) compared with N-M(Ti) where the current density of  $10 \text{ mA/cm}^2$  was set as the reference standard [58,59]. Based on the above analysis, the catalytic mechanisms in uranium reduction via AgNW/N-M(Ti) are formed. As Ag-NWs bonded with N-M(Ti), Schottky barrier, depletion region on the interface of Ag-NWs and N-M(Ti), and band bending were generated due to the transfer of  $e^-$  from N-M(Ti) to Ag-NWs. With the absorption of light, radiative decay and nonradiative decay occurred as plasmon-induced resonant energy transfer (PIRET) and electron-hole pairs ( $e^-/h^+$ ) (Eq. 1). The  $e^-/h^+$  resulting in the heating of plasmonic material (Ag-NWs) and hot carrier injection into the semiconductor (N-M(Ti)) in the meantime [60]. The plasmon-induced resonant energy and light drove and enhanced the generation of  $e^-$  and  $h^+$  by N-M(Ti) (Eq. 2). Then the amino surface of N-M(Ti) selectively captured U(VI) in the wastewater. The  $h^+$  was extracted by N-M(Ti) to oxidize water (Eq. 3), and the  $e^-$  extracted by N-M(Ti) and LSPR from Ag-NWs on the conduction band reduced U(VI) and further generated  $\cdot\text{O}_2$  (Eqs. 4, 5). Finally, U(IV) was converted to a stable crystal phase of  $\text{UO}_4 \cdot 4\text{H}_2\text{O}$  (Eq. 6). This construct of plasmonic metal and semiconductor improved the efficiency of  $e^-/h^+$  and contributed to the photoreduction of U(VI), meanwhile, promoted the enhancement of photothermal mechanism.



## 4. Conclusion

In conclusion, AgNW/N-M(Ti) was successfully constructed as high

activity and stability catalyst for U(VI) photoreduction without any sacrificial agents. A remarkable U(VI) removal ratio (90.4%) was made via AgNW/N-M(Ti) which was introduced with Ag-NWs and strengthened the light-absorbing properties in U(VI) solutions with different concentrations, pH values, and coexisting ions. Even under the influence of F<sup>-</sup> in the U(VI) photoreduction process, AgNW/N-M(Ti) also gained an impressive removal ratio (95.01%), which implied the potential application of the catalyst in fluorine-containing and uranium-containing photocatalytic environments. This work not only provides a photocatalyst for uranium enrichment under simulated light without any sacrificial agent but also introduces a novel MOF material mechanism for advancing the efficient catalytic reduction of uranium in fluorine-containing environments.

## CRediT authorship contribution statement

**Boyuan Tu:** Conceptualization, Methodology, Investigation, Writing – original draft preparation, Writing – review & editing; **Kaifu Yu:** Writing – original draft preparation; **Mingzhe Li:** Methodology; **Li Zhou:** Validation, Methodology; **Ruixiang Wang:** Validation, **Xinying Jiang:** Validation, **Huanhuan Liu:** Methodology; **Xin Cao:** Methodology; **Xiang Gong:** Methodology; **Rong He:** Supervision, Resources; **Yongjian Tang:** Supervision; **Tao Chen:** Project administration, Writing – review & editing; **Wenkun Zhu:** Funding acquisition, Resources.

## Declaration of Competing Interest

The authors declare that they have no known competing financial interests or personal relationships that could have appeared to influence the work reported in this paper.

## Data availability

Data will be made available on request.

## Acknowledgements

This work was supported by NSFC (No. 21976147, U2267224, and 22106126), Sichuan Science and Technology Program (No. 2021YFG0096, 2022YFG0371, and 2022JDRC0074), the Project of State Key Laboratory of Environment-friendly Energy Materials in SWUST (No. 21fksy22). The author would like to thank Shiyanjia Lab ([www.shiyanjia.com](http://www.shiyanjia.com)) for TEM, XPS, and PL analysis and Suzhou Deyo Bot Advanced Materials Co., Ltd. ([www.szdybc.com](http://www.szdybc.com)) for EPR analysis.

## Appendix A. Supporting information

Supplementary data associated with this article can be found in the online version at doi:10.1016/j.apcatb.2023.122965.

## References

- [1] Y. Wu, Y. Xie, X. Liu, Y. Li, J. Wang, Z. Chen, H. Yang, B. Hu, C. Shen, Z. Tang, Q. Huang, X. Wang, Functional nanomaterials for selective uranium recovery from seawater: material design, extraction properties and mechanisms, *Coordination Chemistry Reviews* 483 (2023), 215097.
- [2] M. Hao, Y. Liu, W. Wu, S. Wang, X. Yang, Z. Chen, Z. Tang, Q. Huang, S. Wang, H. Yang, X. Wang, Advanced porous adsorbents for radionuclides elimination, *EnergyChem* (2023), 100101.
- [3] T. Chen, T. Liu, L. Zhou, M. Li, Q. Meng, K. Yu, J. Lian, W. Zhu, Ternary boron carbon nitrides hollow nanotubes with tunable p-n homojunction for photo-assisted uranium extraction: a combined batch, EXAFS and DFT calculations, *Appl. Catal. B Environ.* 318 (2022), 121815.
- [4] X. Wang, X. Dai, C. Shi, J. Wan, M.A. Silver, L. Zhang, L. Chen, X. Yi, B. Chen, D. Zhang, K. Yang, J. Diwu, J. Wang, Y. Xu, R. Zhou, Z. Chai, S. Wang, A 3,2-hydroxypyridinone-based decoration agent that removes uranium from bones in vivo, *Nat. Commun.* 10 (2019) 2570.
- [5] Z. Li, Z. Huang, W. Guo, L. Wang, L. Zheng, Z. Chai, W. Shi, Enhanced photocatalytic removal of uranium(VI) from aqueous solution by magnetic  $\text{TiO}_2/\text{Fe}_3\text{O}_4$  and its graphene composite, *Environ. Sci. Technol.* 51 (2017) 5666–5674.

- [6] P. Liang, L. Yuan, H. Deng, X. Wang, L. Wang, Z. Li, S. Luo, W. Shi, Photocatalytic reduction of uranium(VI) by magnetic ZnFe<sub>2</sub>O<sub>4</sub> under visible light, *Appl. Catal. B Environ.* 267 (2020), 118688.
- [7] P. Zhang, L. Wang, L. Yuan, J. Lan, Z. Chai, W. Shi, Sorption of Eu(III) on MXene-derived titanate structures: the effect of nano-confined space, *Chem. Eng. J.* 370 (2019) 1200–1209.
- [8] L. Feng, Y. Yuan, B. Yan, T. Feng, Y. Jian, J. Zhang, W. Sun, K. Lin, G. Luo, N. Wang, Halogen hydrogen-bonded organic framework (XHOE) constructed by singlet open-shell diradical for efficient photoreduction of U(VI), *Nat. Commun.* 13 (2022) 1389.
- [9] M. Chen, T. Liu, X. Zhang, R. Zhang, S. Tang, Y. Yuan, Z. Xie, Y. Liu, H. Wang, K. V. Fedorovich, N. Wang, Photoinduced enhancement of uranium extraction from seawater by MOF/black phosphorus quantum dots heterojunction anchored on cellulose nanofiber aerogel, *Adv. Funct. Mater.* 31 (2021), 2100106.
- [10] D. Wang, J. Song, S. Lin, J. Wen, C. Ma, Y. Yuan, M. Lei, X. Wang, N. Wang, H. Wu, A marine-inspired hybrid sponge for highly efficient uranium extraction from seawater, *Adv. Funct. Mater.* 29 (2019), 1901009.
- [11] H. Zhang, W. Liu, A. Li, D. Zhang, X. Li, F. Zhai, L. Chen, L. Chen, Y. Wang, S. Wang, Three mechanisms in one material: Uranium capture by a polyoxometalate–organic framework through combined complexation, chemical reduction, and photocatalytic reduction, *Angew. Chem. Int. Ed.* 58 (2019) 16110–16114.
- [12] Y. Zhang, M. Zhu, S. Zhang, Y. Cai, Z. Lv, M. Fang, X. Tan, X. Wang, Highly efficient removal of U(VI) by the photoreduction of SnO<sub>2</sub>/CdCO<sub>3</sub>/CdS nanocomposite under visible light irradiation, *Appl. Catal. B Environ.* 279 (2020), 119390.
- [13] T. Chen, T. Liu, B. Pang, T. Ding, W. Zhang, X. Shen, D. Wu, L. Wang, X. Liu, Q. Luo, W. Zhu, T. Yao, Actinide-uranium single-atom catalysis for electrochemical nitrogen fixation, *Sci. Bull.* 67 (2022) 2001–2012.
- [14] T. Chen, K. Yu, C. Dong, X. Yuan, X. Gong, J. Lian, X. Cao, M. Li, L. Zhou, B. Hu, R. He, W. Zhu, X. Wang, Advanced photocatalysts for uranium extraction: elaborate design and future perspectives, *Coord. Chem. Rev.* 467 (2022), 214615.
- [15] J. Shen, A. Schäfer, Removal of fluoride and uranium by nanofiltration and reverse osmosis: a review, *Chemosphere* 117 (2014) 679–691.
- [16] K. Yu, P. Jiang, H. Yuan, R. He, W. Zhu, L. Wang, Cu-based nanocrystals on ZnO for uranium photoreduction: plasmon-assisted activity and entropy-driven stability, *Appl. Catal. B Environ.* 288 (2021), 119978.
- [17] Q. He, Y. Fu, X. Ge, A. Al-Enizi, A. Nafady, Q. Wang, S. Ma, Facile fabrication of Fe-BDC/Fe-2MI heterojunction with boosted photocatalytic activity for Cr(VI) Reduction, *J. Environ. Chem. Eng.* 9 (2021), 105961.
- [18] Y.A. Bhembe, L.N. Dlamini, Photoreduction of chromium (VI) by a composite of niobium (V) oxide impregnated with a Ti-based MOF, *J. Environ. Sci. Heal. A.* 55 (2020) 1003–1020.
- [19] J. Li, Z. Lou, B. Li, Nanostructured materials with localized surface plasmon resonance for photocatalysis, *Chinese Chem. Lett.* 33 (2022) 1154–1168.
- [20] Y.W. Koh, K. Westerman, S. Manzhos, A computational study of adsorption and vibrations of UF<sub>6</sub> on graphene derivatives: conditions for 2D enrichment, *Carbon* 81 (2015) 800–806.
- [21] R. Zhang, M. Engholm, Recent progress on the fabrication and properties of silver nanowire-based transparent electrodes, *Nanomaterials* 8 (2018) 628.
- [22] H. Lee, Y. Kim, J. Kim, S. Yoon, T. Kim, J. Noh, K. Suh, Synthesis of dimension-controlled silver nanowires for highly conductive and transparent nanowire films, *Acta Mater.* 83 (2015) 84–90.
- [23] L. Song, C. Xue, H. Xia, S. Qiu, L. Sun, H. Chen, Effects of alkali metal (Li, Na, and K) incorporation in NH<sub>2</sub>-MIL125(Ti) on the performance of CO<sub>2</sub> adsorption, *Materials* 12 (2019) 844.
- [24] H. Liu, J. Zhang, D. Ao, Construction of heterostructured ZnIn<sub>2</sub>S<sub>4</sub>@NH<sub>2</sub>-MIL-125 (Ti) nanocomposites for visible-light-driven H<sub>2</sub> production, *Appl. Catal. B Environ.* 221 (2018) 433–442.
- [25] H. Wang, X. Yuan, Y. Wu, G. Zeng, X. Chen, L. Leng, Z. Wu, L. Jiang, H. Li, Facile synthesis of amino-functionalized titanium metal-organic frameworks and their superior visible-light photocatalytic activity for Cr(VI) reduction, *J. Hazard. Mater.* 286 (2015) 187–194.
- [26] X. Chen, Y. Zhang, X. Kong, Z. Guo, W. Xu, Z. Fang, S. Wang, L. Liu, Y. Liu, J. Zhang, Controlling crystal growth of MIL-100(Fe) on Ag nanowire surface for optimizing catalytic performance, *RSC Adv.* 10 (2020) 25260–25265.
- [27] S. Chen, G. Hai, H. Gao, X. Chen, A. Li, X. Zhang, W. Dong, Modulation of the charge transfer behavior of Ni(II)-doped NH<sub>2</sub>-MIL-125(Ti): regulation of Ni ions content and enhanced photocatalytic CO<sub>2</sub> reduction performance, *Chem. Eng. J.* 406 (2021), 126886.
- [28] H. Li, F. Qin, Z. Yang, X. Cui, J. Wang, L. Zhang, New reaction pathway induced by plasmon for selective benzyl alcohol oxidation on BiOCl possessing oxygen vacancies, *J. Am. Chem. Soc.* 139 (2017) 3513–3521.
- [29] Z. Chen, J. Wang, M. Hao, Y. Xie, X. Liu, H. Yang, G.I.N. Waterhouse, X. Wang, S. Ma, Tuning excited state electronic structure and charge transport in covalent organic frameworks for enhanced photocatalytic performance, *Nat. Commun.* 14 (2023) 1106.
- [30] M. Hao, Y. Xie, X. Liu, Z. Chen, H. Yang, G.I.N. Waterhouse, S. Ma, X. Wang, Modulating uranium extraction performance of multivariate covalent organic frameworks through donor–acceptor linkers and amidoxime nanotraps, *JACS Au* 3 (2023) 239–251.
- [31] R.S. Dariani, N. Rahmani, Intraband light absorption in free-standing porous silicon, *Eur. Phys. J. Appl. Phys.* 54 (2011) 21301.
- [32] J. Chen, X. Xu, Y. Ma, H. Qin, J. Liu, F. Lv, C. Zhu, L. Wang, L. Long, F. Liu, Y. Yang, W. Kong, Effects of pyridine-like and pyrrole-like nitrogen on the photoluminescence blue-shift of nitrogen-doped graphene oxide quantum dots, *J. Lumin.* 235 (2021), 117983.
- [33] P. He, L. Zhang, L. Wu, S. Xiao, X. Ren, R. He, X. Yang, R. Liu, T. Duan, Synergy of oxygen vacancies and thermoelectric effect enhances uranium(VI) photoreduction, *Appl. Catal. B Environ.* 322 (2023), 122087.
- [34] G. Luo, Z. Zhang, J. Wang, M. Huang, Y. Long, Y. Liu, Z. Zeng, Y. Wang, J. Zou, A. Ren, S. Luo, Y. Yang, W. Li, H. Lin, D. Zhao, High-performance ultraviolet photodetectors enabled by van der Waals Schottky junction based on TiO<sub>2</sub> nanorod arrays/Au-modulated Ti<sub>3</sub>C<sub>2</sub>T<sub>x</sub> MXene, *Adv. Funct. Mater.* (2023), 2211610.
- [35] M. Wu, H. Liao, Y. Cho, G. Tóth, Y. Chen, W. Su, K. Kordás, Photo-kelvin probe force microscopy for photocatalytic performance characterization of single filament of TiO<sub>2</sub> nanofiber photocatalysts, *J. Mater. Chem. A* 1 (2013) 5715–5720.
- [36] L. Lin, Y. Ma, J. Wu, F. Pang, J. Ge, S. Sui, Y. Yao, R. Qi, Y. Cheng, C. Duan, J. Chu, R. Huang, Origin of photocatalytic activity in Ti<sup>4+</sup>/Ti<sup>3+</sup> core-shell titanium oxide nanocrystals, *J. Phys. Chem. C* 123 (2019) 20949–20959.
- [37] Y. Jiang, Y. Wang, Z. Zhang, Z. Dong, J. Xu, 2D/2D CsPbBr<sub>3</sub>/BiOCl heterojunction with an S-scheme charge transfer for boosting the photocatalytic conversion of CO<sub>2</sub>, *Inorg. Chem.* 61 (2022) 10557–10566.
- [38] X. Wang, Y. Huang, J. Liao, Y. Jiang, L. Zhou, X. Zhang, H. Chen, D. Kuang, In situ construction of a Cs<sub>2</sub>SnI<sub>6</sub> perovskite nanocrystal/SnS<sub>2</sub> nanosheet heterojunction with boosted interfacial charge transfer, *J. Am. Chem. Soc.* 141 (2019) 13434–13441.
- [39] R. Kumar, D. Varandani, B. Mehta, Nanoscale interface formation and charge transfer in graphene/silicon Schottky junctions; KPDM and CAFM studies, *Carbon* 98 (2016) 41–49.
- [40] K. Yu, P. Jiang, J. Wei, H. Yuan, Y. Xin, R. He, L. Wang, W. Zhu, Enhanced uranium photoreduction on Ti<sub>3</sub>C<sub>2</sub>T<sub>x</sub> MXene by modulation of surface functional groups and deposition of plasmonic metal nanoparticles, *J. Hazard. Mater.* 426 (2022), 127823.
- [41] K. Yu, L. Tang, X. Cao, Z. Guo, Y. Zhang, N. Li, C. Dong, X. Gong, T. Chen, R. He, W. Zhu, Semiconducting metal–organic frameworks decorated with spatially separated dual cocatalysts for efficient uranium(VI) photoreduction, *Adv. Funct. Mater.* 32 (2022), 2200315.
- [42] J. Lei, H. Liu, C. Yuan, Q. Chen, J. Liu, F. Wen, X. Jiang, W. Deng, X. Cui, T. Duan, W. Zhu, R. He, Enhanced photoreduction of U(VI) on WO<sub>3</sub> nanosheets by oxygen defect engineering, *Chem. Eng. J.* 416 (2021), 129164.
- [43] C. Dong, T. Qiao, Y. Huang, X. Yuan, J. Lian, T. Duan, W. Zhu, R. He, Efficient photocatalytic extraction of uranium over ethylenediamine capped cadmium sulfide telluride nanobelts, *ACS Appl. Mater. Interf.* 13 (2021) 11968–11976.
- [44] X. Cao, K. Yu, Y. Zhang, N. Li, P. Wang, L. Zhou, X. Gong, H. Wang, F. Yang, W. Zhu, R. He, Efficient strategy for U(VI) photoreduction: Simultaneous construction of U(VI) confinement sites and water oxidation sites, *ACS Appl. Mater. Interf.* 15 (2023) 1063–1072.
- [45] S. Bai, X. Li, Q. Kong, R. Long, C. Wang, J. Jiang, Y. Xiong, Toward enhanced photocatalytic oxygen evolution: synergistic utilization of plasmonic effect and Schottky junction via interfacing facet selection, *Adv. Mater.* 27 (2015) 3444–3452.
- [46] Q. Wang, K. Domen, Particulate Photocatalysts for light-driven water splitting: mechanisms, challenges, and design strategies, *Chem. Rev.* 120 (2020) 919–985.
- [47] Y. Yang, Z. Zeng, G. Zeng, D. Huang, R. Xiao, C. Zhang, C. Zhou, W. Xiong, W. Wang, M. Cheng, W. Xue, H. Guo, X. Tang, D. He, Ti<sub>3</sub>C<sub>2</sub> MXene/porous g-C<sub>3</sub>N<sub>4</sub> interfacial Schottky junction for boosting spatial charge separation in photocatalytic H<sub>2</sub>O<sub>2</sub> production, *Appl. Catal. B: Environ.* 258 (2019), 117956.
- [48] S. Li, P. Miao, Y. Zhang, J. Wu, B. Zhang, Y. Du, X. Han, J. Sun, P. Xu, Recent advances in plasmonic nanostructures for enhanced photocatalysis and electrocatalysis, *Adv. Mater.* 33 (2021), 2000086.
- [49] M. Li, R. Wang, T. Liu, Q. Chen, N. Li, L. Zhou, K. Yu, H. Liu, X. Gong, R. He, F. Ahmad, F. Yang, W. Zhu, T. Chen, Integrating surface functional modification and energy-level adapted coupling of photocatalyst with ultrafast carrier separation for uranium extraction, *Sep. Purif. Technol.* 309 (2023), 123121.
- [50] R. Wang, M. Li, T. Liu, X. Li, L. Zhou, L. Tang, C. Gong, X. Gong, K. Yu, N. Li, W. Zhu, T. Chen, Encapsulating carbon-coated nano zero-valent iron particles with biomass-derived carbon aerogel for efficient uranium extraction from uranium-containing wastewater, *J. Clean. Prod.* 364 (2022), 132654.
- [51] X. Gong, L. Tang, R. Wang, Z. Guo, P. Huang, L. Zhou, J. Zou, J. Lei, H. Liu, N. Li, X. Tang, W. Zhu, R. He, Achieving efficient photocatalytic uranium extraction within a record short period of 3 min by up-conversion erbium doped ZnO nanosheets, *Chem. Eng. J.* 450 (2022), 138044.
- [52] J. Wang, Y. Wang, W. Wang, T. Peng, J. Liang, P. Li, D. Pan, Q. Fan, W. Wu, Visible light driven Ti<sup>3+</sup> self-doped TiO<sub>2</sub> for adsorption-photocatalysis of aqueous U(VI), *Environ. Pollut.* 262 (2020), 114373.
- [53] S. Li, X. Yang, Z. Cui, Y. Xu, Z. Niu, P. Li, D. Pan, W. Wu, Efficient photoreduction strategy for uranium immobilization based on graphite carbon nitride/perovskite oxide heterojunction nanocomposites, *Appl. Catal. B Environ.* 298 (2021), 120625.
- [54] K. Yu, S. Wang, Q. Li, T. Hou, Y. Xin, R. He, W. Zhang, S. Liang, L. Wang, W. Zhu, Au atoms doped in Ti<sub>3</sub>C<sub>2</sub>T<sub>x</sub> MXene: benefiting recovery of oxygen vacancies towards photocatalytic aerobic oxidation, *Nano Res.* 15 (2022) 2862–2869.
- [55] J. Zhang, T. Bai, H. Huang, M. Yu, X. Fan, Z. Chang, X. Bu, Metal–organic-framework-based photocatalysts optimized by spatially separated cocatalysts for overall water splitting, *Adv. Mater.* 32 (2020), 2004747.
- [56] C. Dong, M. Xing, J. Zhang, Double-cocatalysts promote charge separation efficiency in CO<sub>2</sub> photoreduction: spatial location matters, *Mater. Horiz.* 3 (2016) 608–612.
- [57] K. Khan, X. Tao, Y. Zhao, B. Zeng, M. Shi, N. Ta, J. Li, X. Jin, R. Li, C. Li, Spatial separation of dual-cocatalysts on one-dimensional semiconductors for photocatalytic hydrogen production, *J. Mater. Chem. A* 7 (2019) 15607–15614.
- [58] H. Liu, J. Lei, S. Yang, F. Qin, L. Cui, Y. Kong, X. Zheng, T. Duan, W. Zhu, R. He, Boosting the oxygen evolution activity over cobalt nitride nanosheets through

- optimizing the electronic configuration, *Appl. Catal. B Environ.* 286 (2021), 119894.
- [59] F. Zhou, A. Izgorodin, R. Hocking, L. Spiccia, D. MacFarlane, Electrodeposited  $\text{MnO}_x$  films from ionic liquid for electrocatalytic water oxidation, *Adv. Energy Mater.* 2 (2012) 1013–1021.
- [60] L. Mascaretti, A. Dutta, Š. Kment, V.M. Shalae, A. Boltasseva, R. Zboril, A. Naldoni, Plasmon-enhanced photoelectrochemical water splitting for efficient renewable energy storage, *Adv. Mater.* 31 (2019), 1805513.